Climate patterns and surface methane distribution explained by coupling of land hydrology and atmosphere in Titan's methane cycle

Sean P. Faulk[1†], Juan M. Lora[1,2†*], Jonathan L. Mitchell[1,3], P.C.D. Milly[4]

[1]Department of Earth, Planetary, and Space Sciences, University of California, Los Angeles, CA

[2]Department of Geology and Geophysics, Yale University, New Haven, CT

[3]Department of Atmospheric and Oceanic Sciences, University of California, Los Angeles, CA

[4]U.S. Geological Survey, Princeton, NJ

[†]Equal-contribution authors

[*]Corresponding author: juan.lora@yale.edu

Terrestrial planetary surfaces beyond Earth's are noticeably impacted by surface hydrology: Mars and Titan both exhibit widespread fluvial and lacustrine features. Surface hydrology components essential to Earth's hydrologic cycle—including surface and subsurface flow, infiltration, and evaporation from soil—may therefore be similarly influential on other planetary bodies. Titan in particular harbors a rich hydroclimate comparable to Earth's, replete with valley networks, lakes, seas, and putative wetlands, all of which are pronounced in the lower elevation polar regions. However, understanding of Titan's global climate has heretofore largely neglected basic representations of surface hydrology, and therefore neglected the hydraulic influence of Titan's large-scale topography. Here we add a surface hydrology model to an existing Titan atmospheric model, and find that infiltration, groundmethane evaporation, and surface and subsurface flow are fundamental to simultaneously reproducing Titan's observed surface liquid distribution and other aspects of its climate system. We propose that Titan's climate features infiltration into unsaturated low- and mid-latitude highlands and surface or subsurface flow into high-latitude basins, producing the observed polar moist climes and equatorial deserts. This result implies a potentially massive unobserved methane reservoir participates in Titan's methane cycle. It also illustrates the importance of parameterizing surface hydrology in Titan climate models, and by extension suggests the influence of surface hydrology in idealized models of other planetary climates, including the climates and paleoclimates of Earth, Mars, and exoplanets.

Titan's hydroclimate appears especially driven by large-scale topography, given the coincidence of active drainage[1–3], erosional modification[4,5], saturated sediments[6], and seemingly stable lacustrine features[7–9] in the low-lying polar regions. Polar lakes and seas have been interpreted as surface expressions of a continuous, connected "methane table" intersecting with the surface[10]. Persistent solstitial cloud activity[11] and substantial near-surface humidity levels[12,13] concentrated at the poles further indicate a broadly dichotomous world with two climate zones, namely the dry low-latitude highlands and moist polar lowlands[14]. Yet no Titan GCM to date has employed a surface hydrology scheme that accounts for Titan's

large-scale topographic structure, and previous models have failed to reproduce both the observed surface liquid distribution and features of the climate (like the frequency of clouds and distribution of surface temperatures) simultaneously, thus leaving open the question of what processes ultimately control the location of Titan's lakes and seas, and how these affect the global climate. The current model configuration most consistent with cloud observations forces a climate dichotomy by imposing low-latitude infiltration and inexhaustible high-latitude surface methane reservoirs[14,15], illustrating the need for a global surface hydrology model coupled to the atmosphere.

A vast collection of observations bespeaks a surface on Titan as hydrologically rich and complex as its atmosphere. Extensive evidence for erosion and sediment transport from fluid runoff following precipitation events[16–20] indicates the widespread presence of overland flow. At the same time, putative shoreline changes and surface alterations[21–23], geomorphological mapping indicating local hydraulic connectivity[6,10,24], weather patterns[25], and low-level humidity measurements implying methane reservoirs in excess of observed surface liquids[13] all indicate the presence of subsurface methane in communication with the global climate system.

In this study, we present a comprehensive surface hydrology scheme that includes simple and modular parameterizations of overland surface flow, infiltration, subsurface flow, and groundmethane evaporation (Fig. 1a shows a schematic of the model processes), and incorporate it into an existing GCM, the Titan Atmospheric Model (TAM)[26]. For the first time, this fully coupled three-dimensional atmosphere and land climate model allows methane to distribute itself within the climate system self-consistently (see Methods for model details). Recent GCMs have begun to consider hydrology schemes for Titan[15,26–29], but ignoring key features like the hydraulic influence of topography. Likewise, more comprehensive land hydrology modeling has been applied to Titan's north polar region[30], but externally driven by fluxes from an uncoupled GCM. Critically, no previous model has considered the two-way coupling between realistic land hydrology—including transport of liquids—and the atmosphere. Implementing physically self-consistent hydrology leads our model to, for the first time, reproduce Titan's observed regional surface liquids at the same time as observed cloud

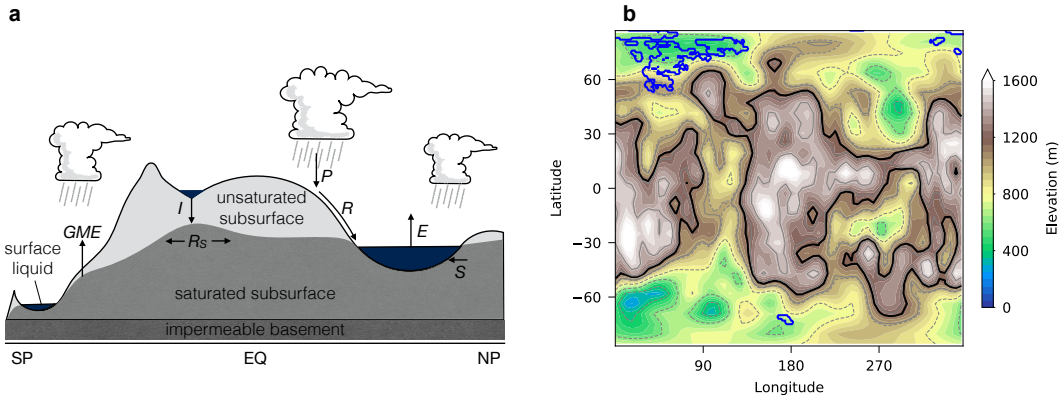

Figure 1: Surface hydrology model and topography map. a) Schematic of the surface hydrology components and processes incorporated in our climate model. A representative longitude slice is shown, with unsaturated low-latitude highlands and saturated high-latitude lowlands. Light grey represents unsaturated subsurface, grey represents methane table, and dark grey represents impermeable basement; dark blue represents surface liquid. Transport processes include groundmethane evaporation (GME), infiltration (I), horizontal subsurface flow of the methane table (R_s) and its special case of seepage onto the surface (S), precipitation (P), surface runoff (R), and evaporation (E), all in units of length per time. Note that the unsaturated subsurface is not a reservoir and does not contain liquid (see Methods text for full description of hydrology model). b) Filled color contours show global elevation (m) above the topographic minimum, from Corlies et al. (2017)[33], interpolated to the resolution of our simulations. Grey contours show normalized elevation, with solid lines indicating above-average elevation and dashed lines below-average elevation. Black contour represents constant equipotential (1200 m) used to initialize the methane reservoir. Thin blue contours show the outlines of the largest observed seas and lakes, for reference.

distributions.

Using our coupled model, we simulate Titan's climate system using different surface permeabilities, spanning the range previously estimated for Titan[8,21,30], in order to determine whether a stable and realistic climate configuration is possible with our self-consistent configuration, and what that can tell us about Titan's methane cycle. Five simulations are initialized identically (see Methods), and each run for a total of 250 Titan years (approximately 7,375 Earth years) to allow the hydrologic cycle time to equilibrate. The results are compared in the following, using averages from the final 20 Titan years of each simulation except where noted.

Surface and subsurface liquid distributions

The principal criterion for evaluating our simulations is whether or not any reproduce the basic aspects of Titan's observed distribution of methane lakes and seas[8,9]. Major seas—Titan's maria, which contain 80% of observed liquid-filled surface area[31]—fill the northern polar basins roughly between 50 and 100°E, and a large lake—Ontario Lacus, which has a large catchment area[32]—exists in the south. While much smaller lakes also exist elsewhere at Titan's north pole, these primary large features dominate and also coincide with some of Titan's large-scale topographic depressions (Fig. 1b). Importantly, many mid-latitude depressions, such as those around 45°N, 60°E and 60°S, 20°E, were not observed by Cassini to contain surface liquid, though some in the dry southern hemisphere have been interpreted as empty paleoseas[9,24].

Of our simulations, the three with the lowest surface permeabilities all reproduce large-scale surface liquid distributions that are congruent with observations (Fig. 2a–c). Deep reservoirs fill the regions occupied by Titan's maria as well as the catchment basin of Ontario Lacus. In all cases there is also some liquid that occurs in the deepest depression, in the southern hemisphere, though it is smaller in scale. In the case with the lowest permeability, some liquid also exists at northern high mid-latitudes; in the next lowest, more liquid pools in the southern hemisphere than in the northern. Both of these points contradict observations, so, of these simulations, the best scenario is that produced by the third option (Fig. 2c). On the other hand, the two simulations with higher permeabilities lead to generally unsatisfactory surface liquid distributions that are in clear disagreement with observations of Titan (Fig. 2d–e). The simulation with the highest permeability produces widespread methane oceans with wide expanses of liquid-covered surface even at lower latitudes; the other leads to liquids primarily at mid-latitudes and no obvious buildup at Titan's north pole.

These results are directly tied to the final disposition of the subsurface methane table. In all cases, liquids on the surface are exposures connected to the subsurface (Fig. 3). Elsewhere, the depth of the table relative to the topography is related to the permeability: At the lowest permeability, inefficient infiltration causes a relatively flat and static table with depths in

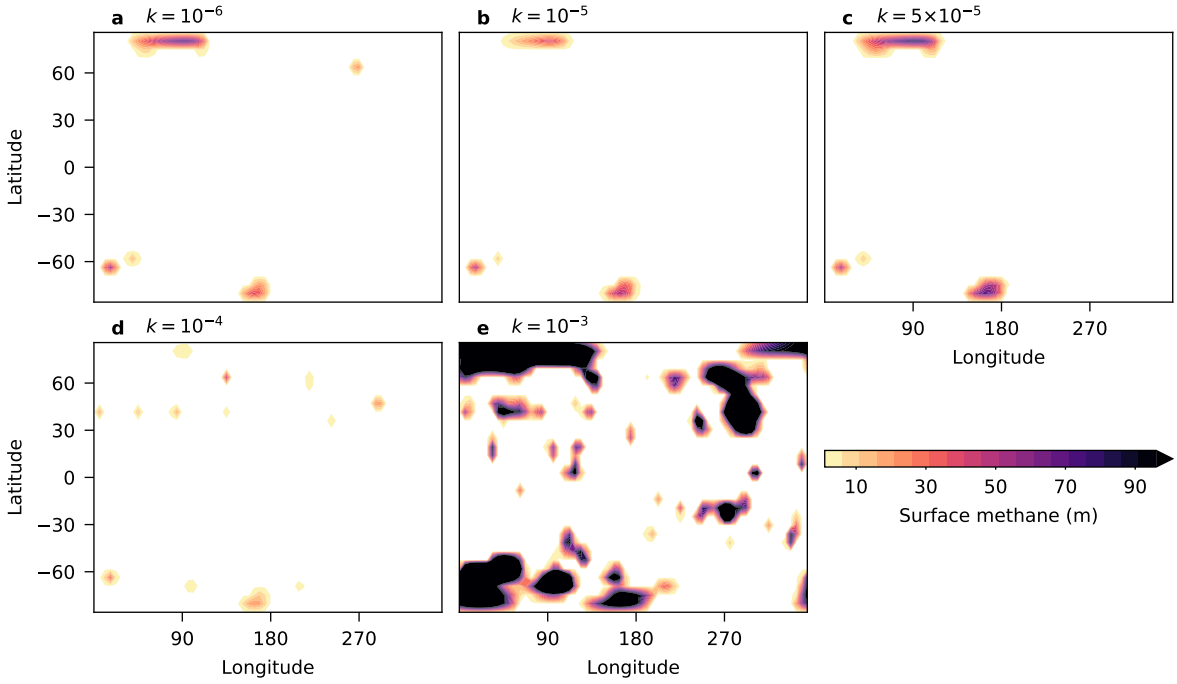

Figure 2: Surface liquid distributions. Distribution of surface liquids (m) averaged over the final 20 Titan years of each simulation. The hydraulic conductivity k of the surface (in units of m s^{-1}) is shown for each case, and corresponds to a permeability of a) 10^{-8} cm^2, b) 10^{-7} cm^2, c) 5×10^{-7} cm^2, d) 10^{-6} cm^2, and e) 10^{-5} cm^2.

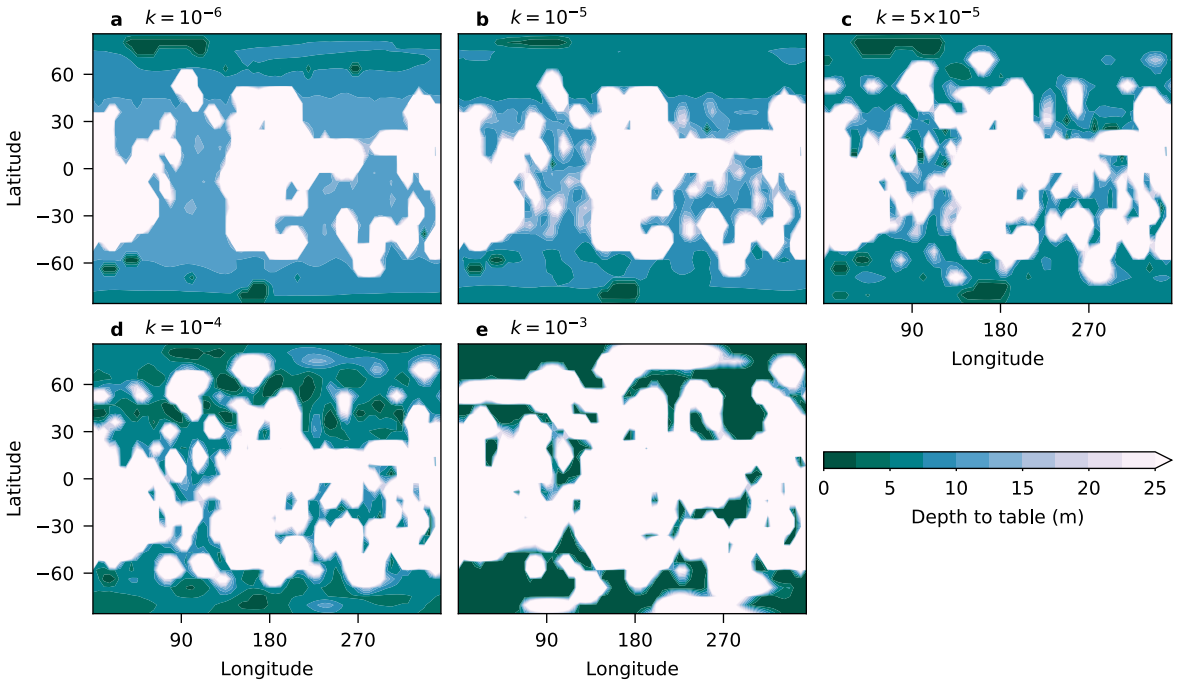

Figure 3: Subsurface methane tables. Maps of the average depth to the methane table (m) over the final 20 Titan years of each simulation. Simulations as in Fig. 2.

excess of 10 m equatorward of about 45°N and 60°S, while at the highest permeability, fast subsurface transport quickly alters the table, preventing it from remaining close to the surface in regions of relatively high topography but producing excessive standing surface liquids in all low-lying areas. In the next-highest case (Fig. 3d), high infiltration rates raise the table at mid-latitude low-lying regions, but subsurface transport is insufficiently fast to further localize it; in this case, the subsurface hydraulic head gradients are largest. With $k = 5 \times 10^{-5}$ m s^{-1}, infiltration at low- and mid-latitudes, combined with surface and subsurface flow poleward, lead to the realistic scenario described above (Fig. 3c).

Precipitation, evaporation, and surface temperatures

A further key test for the realism of our simulations is the accuracy of their resulting hydroclimates relative to observations. As has been done previously for Titan climate models, we rely on precipitation metrics to benchmark against extensive cloud observations (Supple-

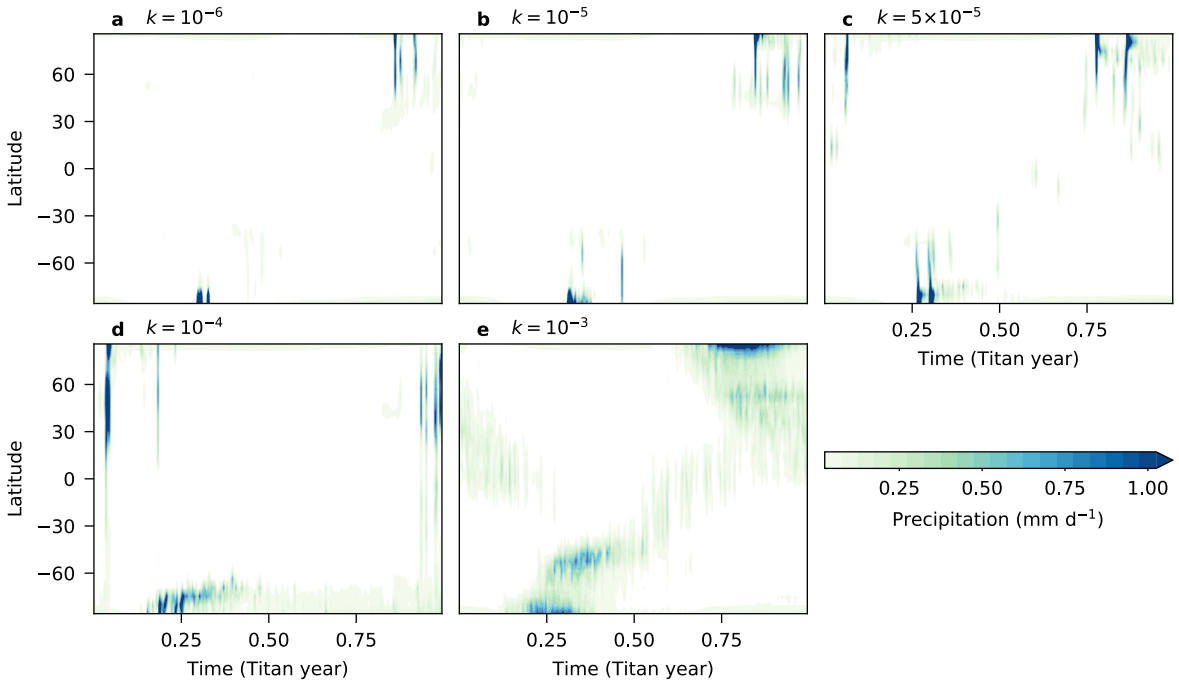

Figure 4: Seasonal precipitation distributions. Zonally averaged precipitation (mm d^{-1}) composited over the final 20 Titan years each simulation. Simulations as in Fig. 2.

mentary Fig. 1), with the inherent assumption that clouds are a prerequisite to precipitation (but recognizing that not all clouds necessarily produce rain; TAM does not currently resolve non-precipitating clouds). Fig. 4 displays the average seasonal precipitation patterns for our climate simulations. The zonal-mean precipitation distributions of all simulations illustrate that our coupled atmosphere–surface hydrology model capably captures the essential aspects of Titan's hydrologic cycle: abundant summertime polar rain, with scattered storms at lower latitudes.

But, of the five, the simulation with $k = 5 \times 10^{-5}$ m s^{-1}—corresponding to a permeability of $\sim 5\times10^{-7}$ cm^2—best captures Titan's present climate (Fig. 4c). The rain distribution of this simulation is similar to that of the model with imposed surface methane distribution[15], which satisfactorily reproduced cloud observations from Cassini instruments and ground-based telescopes[14,20,25], including summertime polar and mid-latitude rain, and isolated low-latitude storms around equinox. That this configuration produces satisfactory

distributions of both surface liquids and precipitation simultaneously is especially compelling, given previous difficulties in reconciling the two[26].

The lower and higher permeability simulations do not reproduce Titan's observed precipitation behavior as satisfactorily. In general, as expected from previous studies demonstrating the hydrologic cycle's dependence on surface liquid distribution[26,27,34], more rain occurs in simulations with more methane available to the atmosphere; in our simulations, atmospheric methane is strongly linked to the permeability of the surface (Supplementary Fig. 2a). As such, in the highest permeability case, abundant surface liquids promote rain at nearly all latitudes, with particularly excessive southern mid-latitude rain during solstice compared to observations (Fig. 4e). Such a regime features a nearly continuous band of seasonal rain, analogous to Earth's intertropical convergence zone, also reported in previous Titan models with globally wet surfaces[26,28,34,35]. Meanwhile, the precipitation distributions for the two lowest permeability cases lack any low-latitude precipitation during the equinox (Fig. 4a–b), and the remaining case conspicuously lacks Titan's characteristic southern mid-latitude precipitation during the solstice-equinox transition (Fig. 4d).

As with the total atmospheric methane content, the average surface temperatures in our simulations depend on the surface permeability (Supplementary Fig. 2b). This is because more liquid methane is available to the atmosphere at higher permeability, which results in more evaporative cooling, which in turn leads to a colder climate. (Previous work concluded that a lapse-rate feedback is primarily responsible for such a dependence of the surface temperature on whether the climate is dry or moist[27].) In addition, all but the simulation with highest permeability produce equator-to-pole surface temperature gradients of 1–3 K, which are asymmetric between summer and winter hemispheres, as well as seasonal temperature changes at the poles of around 2 K (Fig. 5a–d), in agreement with observations of surface brightness temperatures[36]. In contrast, the simulation with highest permeability and resulting widespread surface liquids produces equator-to-pole contrasts of roughly 2 K, but without asymmetry and with seasonal variations much smaller than 1 K (Fig. 5e).

Measured north polar surface brightness temperatures have been noted to be highly spatially homogeneous, which has been attributed to evaporation from extensive polar reser-

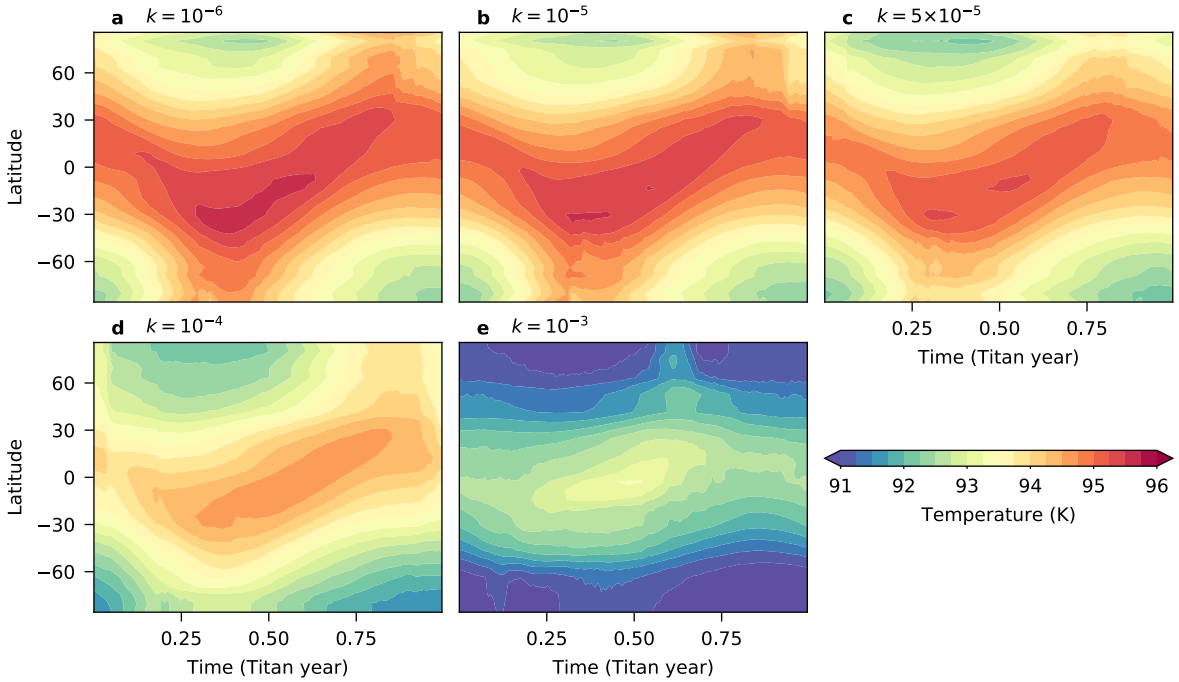

Figure 5: Seasonal temperature distributions. Zonally averaged surface temperatures (K) composited over the final 20 Titan years each simulation. Simulations as in Fig. 2.

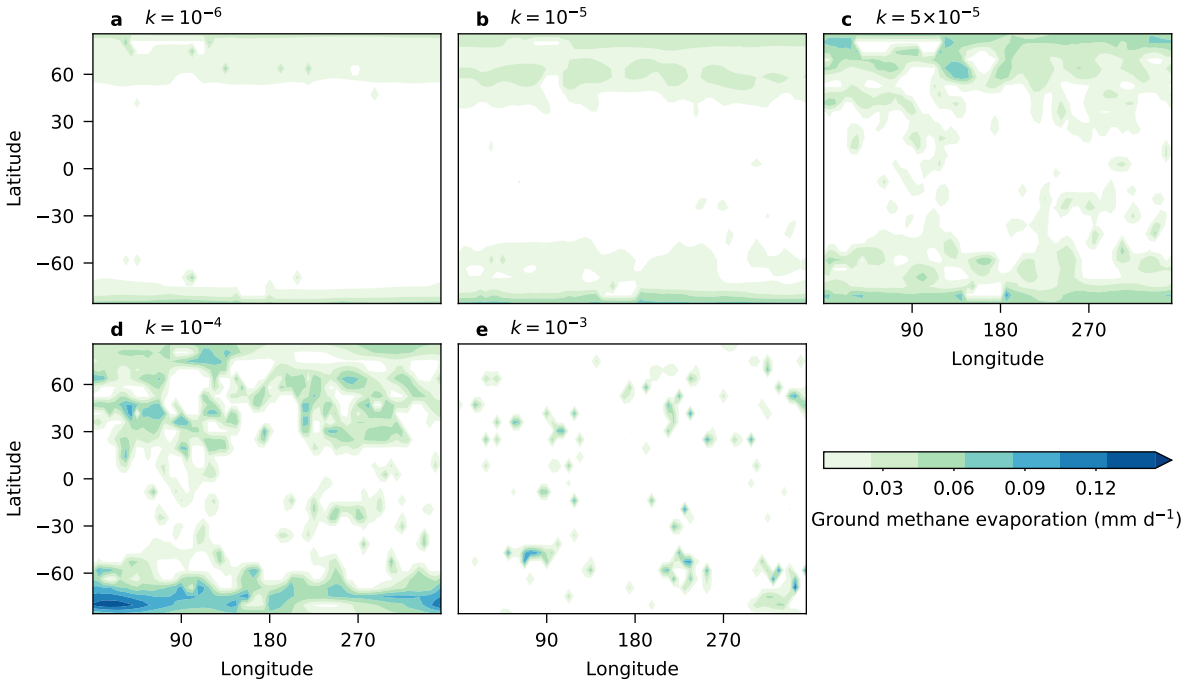

Figure 6: Groundmethane evaporation. Maps of the average groundmethane evaporation (mm d^{-1}) over the final 20 Titan years of each simulation. Simulations as in Fig. 2.

voirs of near-surface methane surrounding the more localized lakes and seas[13,37]. Interestingly, such near-surface reservoirs self-consistently occur in our simulations, particularly in those with intermediate permeabilities (Fig. 3). These contribute to uniform temperatures via groundmethane evaporation in regions of the poles with no surface methane (Fig. 6), which contributes substantially to replenishing the atmospheric methane. In the simulation that produces the best match to observed surface liquids and clouds, this groundmethane evaporation is highest at the poles and slightly hemispherically asymmetric, with larger contributions from the northern hemisphere (Fig. 6c).

Evolution of the surface liquid reservoir

Our simulations demonstrate that Titan's current hydroclimate represents a balance between horizontal transport and vertical surface–atmosphere fluxes of methane. Over long timescales, atmospheric convergence of moisture is balanced locally by net precipitation.

Previous Titan models noted atmospheric moisture divergence from low latitudes[26–28,38,39], but only when the low-latitude surface was wet. With polar liquids as a source, Titan's atmosphere converges methane towards low latitudes[15]. In our coupled model, surface and subsurface transport return methane poleward, with high-latitude evaporation (including groundmethane evaporation) and lower-latitude infiltration closing the cycle (Supplementary Figs. 3–7). With surface permeabilities that are too low, overland flow localizes surface liquids into a realistic distribution, but insufficient methane is available to the atmosphere to maintain the observed cloud activity. On the other hand, with surface permeabilities that are too high, infiltration and/or subsurface transport outpace the other branches of the cycle, and lead to unrealistic surface methane distributions. Therefore, observations of Titan seem to indicate a goldilocks parameter space, which in our current model configuration is attained with $k \approx 5 \times 10^{-5}$ m s^{-1}, corresponding to a global-scale permeability of 5×10^{-7} cm^{-2}. With this value, the model self-consistently establishes a climate with moist poles and dry low latitudes that resembles observations.

Importantly, our simulations reach a quasi-equilibrium of the surface methane budget after approximately 100 Titan years (Supplementary Fig. 8). The exception is the high-permeability simulation, in which the mass of methane on the surface increases asymptotically through the simulation, quickly exceeding the others by about an order of magnitude, and is still increasing by year 250. In the other four, there is not a clear relationship between total surface methane and permeability, but the one that produces the most satisfying match to observations is also the one with the most surface methane, which corresponds to roughly an order of magnitude less mass than is held in the atmosphere (Supplementary Figs. 2a and 8), in agreement with observational estimates[40]. In addition, all cases display notable variability about the long-term average, suggesting the possibility that observable year-to-year variations of lake and sea depth or area might occur on Titan.

Discussion and conclusions

Adding surface hydrology to an existing Titan GCM self-consistently produces a latitudinally dichotomous climate with strong solstitial precipitation over saturated polar regions,

dispersed low-latitude storms, high-latitude maria, and equatorial deserts. The atmosphere deposits methane into the low latitudes to be infiltrated, while surface and subsurface transport routes methane into high-latitude basins, which then feed the atmospheric moisture. In addition, our model demonstrates the importance of near-surface methane, groundmethane evaporation, and surface/subsurface methane transport in Titan's climate. Our results therefore compellingly suggest that a subsurface methane reservoir substantially more massive than the observed seas interacts with the atmosphere and participates in the methane cycle. This may imply a much longer-lasting source of replenishment for Titan's photolytically destroyed methane than previously thought.

Our model does not explain all observations of Titan's methane. In particular, the small lakes that dot the northern polar surface roughly between 30–160°W have no corresponding surface expression in the simulations, though they occur over a relatively shallow methane table. Most of these fill sharp-edged depressions, which indicate unique formation processes[10,41]. Regardless, our current model does not incorporate the direct influence of topography on the atmosphere, which could lead to zonal asymmetries in precipitation (though observations do not appear to support this[11]). Nor does it account for regional variations in surface characteristics, which may be important for such small-scale features. Our best-fit permeability corresponds to materials that on Earth would be pervious or semi-pervious soils, such as well sorted sand, gravel, or peat. While this may be consistent with evidence from the Huygens probe—which landed near the equator on what was interpreted to be wet clay or sand[42]—we can only constrain hydraulic properties and cannot claim to constrain the actual composition of Titan's regolith or underlying bedrock. Indeed, we know that terrestrial and martian materials are composed of a constellation of rock types, each with varying infiltration capacities, permeabilities, and porosities. Radar and spectral observations indicate a similar diversity of materials on Titan, including exposed water ice bedrock, hydrocarbon and nitrile grains, and aerosol dust[43–46]. Separately, while observed surface temperature gradients are captured satisfactorily, the simulations with intermediate permeabilities produce temperatures that are somewhat too warm relative to observed brightness temperatures, indicating slightly insufficient evaporative cooling.

As a result, future work may need to consider a mixture of permeabilities with spatially varying soil parameters, and which might lead to a locally higher methane table. For example, a plausible scenario given our results would be one with relatively higher permeabilities at high latitudes, transitioning to somewhat lower permeabilities at low latitudes. This would result in high amounts of runoff at low latitudes and infiltration at mid-latitudes, preventing ponding there, but also efficient seepage into high-latitude basins, which would increase high- and mid-latitude groundmethane evaporation. In fact, such a distribution would be consistent with the potentially karstic, highly permeable composition suggested for the polar surface[6,10,24,47], as well as the eroded appearance of the low latitudes and unique geomorphic character of mid-latitude zones[3,19,20,31,48].

Several additional lines of research should also be further explored with our new coupled climate model. For example, we will be able to convincingly test the relative influence of changing orbital forcing on the asymmetry of Titan's surface liquids[29,39], as well as on the subsurface. And the distribution of runoff from such simulations, in comparison to observed geomorphology, could shed light on the hydrologic cycle as recorded on the surface through time. Separately, the influence of varying liquid composition (for example, incorporating ethane) on the hydrologic cycle will need to be evaluated, as will the possible connection of a near-surface methane table with putative methane clathrates deeper in Titan's crust[49,50]. Such complexities, and a lack of data constraining them, complicate our understanding of Titan's climate system, but models such as ours can help elucidate its key global properties and processes, particularly in preparation for future *in situ* exploration of Titan with NASA's Dragonfly mission. Direct knowledge of the composition, porosity, and moisture content of Titan's surface—even at select locations—will dramatically constrain our uncertainties and improve understanding of Titan's global hydrologic cycle.

In summary, although large uncertainties remain to be resolved, our model's efficacy in self-consistently reproducing Titan's observed climate state and providing a constraint on Titan's dominant bedrock permeability highlights its utility as a tool for better understanding this complex world. Ongoing work to include the effects of topography on the atmosphere, as well as spatially dependent soil parameters in our model may provide greater insight into

Titan's regional hydroclimate and climate evolution, and future missions to Titan will help characterize the icy satellite's unique lithologic conditions and inform climate model developments. Lastly, our model's capabilities may be relevant in application to other planetary settings with large-scale topography in a hydrologic system with surface–atmosphere coupling, such as the paleoclimates of Titan and Mars, and even Earth. Further work to refine and adapt the model to variable planetary settings will enable ongoing contributions to the emerging field of planetary hydrology.

Correspondence and requests for materials should be addressed to J.M.L.

Acknowledgements

This research was supported by NASA Cassini Data Analysis and Participating Scientists (CDAPS) Program grant NNX16AI44G. We are grateful to A. Hayes for insightful discussions pertaining to groundmethane evaporation, and to S. Moon for thorough and thoughtful comments on earlier versions of the manuscript.

Author Contributions

J.L.M. and J.M.L. devised the study. S.P.F. developed the land hydrology model with input from all authors. S.P.F. and J.M.L. carried out the analysis and prepared the manuscript, with contributions from all authors.

Data Availability

The data that support the findings of this study will be deposited in Zenodo and made available prior to publication.

Methods

TAM The Titan Atmospheric Model (TAM) is a three-dimensional GCM based on the Geophysical Fluid Dynamics Laboratory spectral dynamical core, which has been benchmarked against a variety of observations of Titan's atmosphere and seasonal methane cycle[26]. The model includes a complete physics package to parameterize unresolved processes including a fully nongray radiative transfer code, simplified parameterizations of moist convection to account for subgrid scale deep convection[51] and large-scale condensation when cells exceed saturation, a saturation vapor pressure calculation over methane-nitrogen liquid[13], surface–atmosphere exchange via bulk aerodynamic formulae, and thermal diffusion through the soil.

Here we assume that liquid methane is distributed into three reservoirs: a surface reservoir, as in the original formulation of TAM[26]; a runoff reservoir; and a subsurface reservoir. The surface reservoir represents the lakes and seas of Titan's hydrosphere, sourced by precipitation, runoff, and seepage from the subsurface. The runoff reservoir constitutes surface liquid methane that is "in transit" flowing along topographic gradients and unavailable for atmospheric evaporation, thus representing the river channels and flow networks on Titan's surface. Lastly, the subsurface methane table reservoir constitutes the liquid methane stored underground, representing Titan's saturated zone. The unsaturated zone, or the region of the subsurface between the top of the methane table and the surface topography, is not a reservoir and does not contain liquid. In the following, we describe the steps of the surface hydrology scheme in the order that they are performed in the model. To ensure tractability and robustness, we have designed our model to be self-consistent, meaning that all fluxes within the model are fully interactive, and to be principally dependent on the permeability, so as to avoid an extensive tuning exercise that would diminish the impact of our results.

Implicit in our study is the assumption that the physical properties governing flow in terrestrial settings apply to the ice-grained world of Titan. We argue, however, that despite obvious lithologic differences, Titan's grain size distribution[8,16,30] and overall geomorphologic character[3] are strikingly reminiscent of terrestrial settings, and therefore justify the assump-

tion of correspondingly similar hydrologic mechanisms, including channelized overland flow and flow through pore space and fracture apertures.

Evaporation The first step in the hydrology scheme is to add to each grid cell the net accumulation of methane, calculated as the difference between precipitation and evaporation for a given time step. Evaporative fluxes are calculated using bulk aerodynamic formulae except where the surface is dry, in which case evaporation from the subsurface reservoir—groundmethane evaporation—occurs. Following terrestrial analogs[52–54], we approximate groundmethane evaporation to depend exponentially on depth, such that $GME = E \times exp[A(h - z_t)]$, where z_t is the geoid-corrected topography[33], h is the methane table height relative to a reference equipotential, E is the evaporation of a standard wet surface as calculated by bulk aerodynamic formulae, and A is a specified constant (see Table 1 for a complete list of values used for all hydrology simulations).

Terrestrial groundwater evaporation profiles vary widely and are strongly influenced by vegetation[53,55]. The extinction depth—the depth at which groundwater evaporation becomes negligible—is typically 1–5 meters in terrestrial settings, tending closer to 1 m for bare soil in arid desert regions devoid of vegetation, such as those in the Chilean desert[54]. Given Titan's aridity and lack of vegetation, we set A=1 m^{-1} in our hydrology simulations in order to attain an e-folding depth of 1 m and approximate those typical terrestrial groundwater evaporation profiles in arid and semiarid terrains. Small variations of this parameter do not appreciably affect our results.

Evaporation is additionally impacted by the thermal properties of the soil. We therefore include a vertically resolved soil model with 10 layers of variable thickness. Heat is transported throughout the soil column via conduction[26], with varying thermal properties depending on the presence of liquid. To consider the effect of subsurface methane saturation on the soil temperature, we adjust the thermal conductivity α and heat capacity c_v in each layer at depth z according to whether the methane table has reached that layer's depth. For unsaturated soil at a given depth z, $c_v(z) = \Delta z(z) \times [c_{v,reg}(1-\eta) + c_{v,liq}\eta]$, where $c_{v,reg}$ uses the value for a rock-ice mixture[56] (Table 1). Similarly, $\alpha(z) = \alpha_{reg} \times (1-\eta) + \alpha_{liq}\eta$, where Δz is the layer thickness and η is the porosity, and α_{reg} is chosen based on the results of

MacKenzie et al. (2019)[57]. (Note that adding thermal conductivities linearly is a necessary approximation given the difficulty in discerning a true mixing curve for Titan.) Otherwise, for unsaturated soil, $c_v(z) = \Delta z(z) c_{v,reg}(1-\eta)$ and $\alpha(z) = \alpha_{reg}(1-\eta)$, whereas for lakes and seas, $c_v(z) = \Delta z(z) \times c_{v,liq}$ and $\alpha(z) = \alpha_{liq}$.

Infiltration If after evaporation the surface liquid remains above a specified depth h_i, infiltration occurs. In the limit of infinite time, the infiltration rate of liquid into soil can be approximated as equal to the hydraulic conductivity k, which is proportional to the soil permeability κ with gravity, fluid density, and fluid viscosity as the proportionality constants. We therefore approximate the infiltration rate in our model as equal to the hydraulic conductivity, and perform simulations over a wide range of soil permeabilities estimated for Titan, which translates to hydraulic conductivities between 10^{-6}–10^{-3} m s^{-1} [8,21,30].

The threshold h_i is set at 2 cm in all simulations to represent the initiation of broad-scale runoff and infiltration following large storm events[58]. Infiltration on Earth generally occurs at the expense of runoff during average storm events, so we execute infiltration before runoff in our model (additional simulations show that a reversal of the infiltration-runoff computation order, as well as adjustments to the threshold h_i, lead to negligible changes in the resulting climate). Infiltration in our model occurs anywhere on the globe where the subsurface is unsaturated, and infiltrated methane is immediately added to the methane table regardless of the depth to the table.

Runoff If after infiltration the surface liquid still remains above h_i, we allow horizontal overland flow to the cell of steepest descent[59,60], with flow rates dependent on surface liquid amounts. We choose a steepest-descent method because single flow direction methods in an eight-point grid system enable convergent flow over topography in a fashion that closely approximates downslope flow, and because single flow direction methods represent channel properties in coarse-resolution terrains more suitably than multiple flow direction methods[61,62]. Following terrestrial models and to maintain simplicity, we assume channelized flow such that the area coverage of runoff is much less than the grid cell itself. Thus, evaporation and infiltration can be neglected for liquid that is considered to be within streams or rivers.

Runoff is determined based on each grid cell's potential ϕ in meters, such that $\phi = z_t + h_s$, where again z_t is the topography, and h_s is the surface liquid depth. If the potential ϕ of a given source cell is higher than any one of its eight neighbors, liquid is removed from the surface reservoir of the source cell and added to the runoff reservoir of the cell of steepest descent, which is the cell with the steepest potential gradient $\frac{d\phi}{dl}$ where dl is the centered finite difference distance between the two cells. During the same time step, any liquid in the source cell's runoff reservoir is moved to the runoff reservoir of the cell of steepest descent as well. We restrict outflow from exceeding half the potential difference between the two cells, and we ignore any meandering and unevenness at the subgrid scale, which might alter runoff timescales. For cells at the model's highest latitudes, the three poleward neighboring cells are considered to be the three cells at the same latitude but directly across the pole from the cell in question.

Following Horvath et al. (2016)[30], we calculate the runoff flow rate using a form of the linear reservoir approximation, which assumes that the amount of surface runoff is linearly related to the amount of liquid stored in the catchment[63–68]. As such, the flow Q is given by $Q = \frac{S}{k_s}$, where the storage S is the amount of methane in the surface reservoir in kg m^{-2} and the coefficient k_s is taken as equal to half the concentration time t_c[30,63,65], which is defined as the amount of time in seconds it takes a parcel of liquid to travel the distance of a catchment.

For large terrestrial catchment basins, $t_c = 0.000326(\frac{L}{S_0^{0.5}})^{0.79}$ hrs[64], where L is the length of the catchment in meters and S_0 is the slope. Since basin concentration times decrease with increasing slope, flow is therefore dependent on topographic slope and available methane storage. We consider each grid cell in our model to be a "basin," and assume a constant L of 150 km, the approximate median length of channels observed in the polar regions on Titan[3,30] and an intermediate length scale for grid cells in our model at T21 resolution (roughly 5° horizontal resolution). We take S_0 to be the steepest potential gradient $\frac{d\phi}{dl}$. To modify this terrestrial approximation for Titan, we scale the concentration time by a factor of $\mu/\rho g$, where μ is the dynamic viscosity and ρ is density of liquid, since velocity is proportional to the ratio of gravity to kinematic viscosity and flow time is inversely proportional to

velocity[30].

All together, this approximation gives concentration times between 1–20 days, comparable to basin lag times in terrestrial models[65,69–71]. Corresponding runoff rates therefore span several orders of magnitude, ranging from 10^{-6}–10^{-2} kg m^{-2} s^{-1}, which are typically one or more orders of magnitude greater than evaporation changes when runoff occurs. Note that given Titan's poorly constrained surface materials, basin geometry, and methane flow characteristics, calculating discharge using standard terrestrial methods is not straightforward[3]. Thus, the crucial element to capture when parameterizing runoff speed is that runoff is fast compared to evaporation when there are substantial liquid amounts, which our linear reservoir approximation achieves.

After surface liquid removal and overland flow are calculated for each grid cell, the flow back to the surface reservoir is determined. The liquid in a given cell's runoff reservoir returns to that cell's surface reservoir under the following two conditions: 1) if the methane table at a given grid cell is below the surface but the grid cell lies at a local depression in potential ϕ; and 2) if the methane table at a given grid cell has reached the surface. The second condition is meant to simulate flow to a potentially large sea that immediately becomes available for evaporation at the shoreline. Buildup of methane at any one grid cell is prevented by the fact that runoff is calculated based on the potential of both the topography and the surface liquid height.

Subsurface transport We refer to the subsurface reservoir as always below ground. However, where the soil is saturated to the surface, the effective height of the methane table then reaches above ground and includes contributions from both the saturated subsurface reservoir and the surface reservoir (see Fig. 1a). The height of the methane table is measured relative to the topographic global minimum equipotential. (For simplicity we assume an impermeable basement that is also an equipotential, but this has no effect on subsurface flow.) Differences in the methane table height are then used to calculate horizontal adjustments to the methane table via a finite-difference approximation of the equation for subsurface flow, forms of which have been used in previous Titan studies[30] and are commonly used in terrestrial GCMs with land models[72,73] to calculate liquid flow in porous media.

From Darcy's law, the volume of liquid removed from a source cell is proportional to the head gradient between the source cell and the destination cell. For each of the four flow directions, we have

$$\eta \frac{dh}{dt} = \frac{kbL_c}{A_c} \frac{dh}{dl} \tag{1}$$

where h is the methane table height of the source cell, b is the aquifer thickness (equal to the methane table height of the source cell in our approximation), L_c is the horizontal length of contact between cells, and A_c is the source cell area. For simplicity, hydraulic conductivity in our model is held globally constant, and is isotropic and independent of depth. Therefore, since vertical and horizontal hydraulic conductivities are the same, simulations with low permeability (and thus low hydraulic conductivity) also have correspondingly low infiltration rates.

Flow is calculated in the north–south and east–west directions, thus encompassing a diffusive multiple flow direction method in contrast to the single flow direction method employed for surface flow. Similarly to the overland surface flow scheme, however, we restrict flow in our subsurface flow scheme to not exceed half the table height difference between the source and destination cells, in order to prevent numerical instabilities. Given a cell of high potential, in each of the four directions we calculate the volume of liquid removed, following Darcy's law and the aforementioned restriction to prevent numerical instabilities, and then ensure that the sum of those four volumes is available to be removed. The result is a subsurface transport scheme that conserves methane and produces smooth flattening of methane table profiles, even given permeability parameters that are far outside the expected range for Titan. Our model is therefore functional for generalized planetary hydrology studies in the future.

Topography Throughout the above processes, topography is used only as an input into hydrology calculations, and is not coupled to the atmosphere via orographic effects, which could introduce zonal asymmetries on the distribution of precipitation that we therefore neglect. The topography map used in our study is the most recently updated product

from Cassini RADAR data[33]. Altimetry, SARtopo, and stereophotogrammetry datasets are limited to only 9% of Titan's surface area, so an interpolation is required to generate a full global topographic map. We use the un-smoothed geoid-corrected interpolation of Titan's topography, with the geoid derived from parameters reported by Iess et al. (2012)[74], and further interpolate to T21 resolution for use in our simulations (Fig. 1b). Thus, basins in our topography do not exactly coincide with the observed basins. Nevertheless, given our interest in large-scale climate dynamics, the approximate correlation is suitable for our purposes.

Experimental setup We run all simulations at T21 resolution (64 longitude points by 32 latitude points) with 32 atmospheric vertical layers and a time step Δt of 600 seconds, starting from an atmosphere at rest relative to the solid body. For each simulation, we begin with liquid methane up to an equipotential surface of 1200 meters relative to the topographic minimum. This level was found by trial and error to provide sufficient methane for a robust hydrologic cycle without always leading to global-scale surface liquids. In other words, with an initial methane table at a substantially lower equipotential surface, the hydrologic cycle uniformly shuts down—even with permeabilities at the higher end of the estimated range—and is characterized by insufficient precipitation and warm surface temperatures; with a substantially greater initial methane table, all simulations within the estimated permeability range produce global methane oceans. Thus, the chosen initial methane table amount enables a proper investigation of the influence of permeability on Titan's hydrologic cycle. We set the surface to be initially dry, such that the subsurface is completely saturated wherever the topography is below 1200 meters, but no lakes or seas exist anywhere.

Five simulations with permeabilities spanning three orders of magnitude in the range estimated for Titan are run for 250 Titan years. This run length is chosen to allow the hydrologic cycle time to equilibrate: As an order of magnitude estimate, the radius of Titan divided by a conductivity of $k = 10^{-5}$ m s^{-1} yields a timescale of $\sim$275 Titan years, with larger k implying faster equilibration times. We also tested simulations spanning a larger range of permeabilities, but expectedly these behave similarly to our end members so were not run for the 250 years. That is, a simulation with $k = 10^{-8}$ m s^{-1} produces an inactive

methane table, while one with $k = 10^{-2}$ m s^{-1} immediately results in near-global methane oceans.

Parameter	Description	Value
A	Groundmethane evaporation scaling parameter	1.0 m^{-1}
η	Porosity	0.5
$c_{v,reg}$	Volumetric heat capacity of regolith	2.1 x 10^6 J m^{-3} K^{-1}
$c_{v,liq}$	Volumetric heat capacity of liquid	1.8 x 10^6 J m^{-3} K^{-1}
α_{reg}	Thermal conductivity of regolith	0.5 W m^{-1} K^{-1}
α_{liq}	Thermal conductivity of liquid	0.3 W m^{-1} K^{-1}
h_i	Infiltration/runoff threshold	2 x 10^{-2} m
L	Basin catchment length	1.5 x 10^5 m
ρ	Density of liquid	450 kg m^{-3}

Table 1: Complete hydrology parameter list. See Methods text for full description of surface hydrology scheme.

References

[1] Wall, S. *et al.* Active shoreline of Ontario Lacus, Titan: A morphological study of the lake and its surroundings. *Geophys. Res. Lett.* **37**, L05202 (2010).

[2] Langhans, M. *et al.* Titan's fluvial valleys: Morphology, distribution, and spectral properties. *Planet. Space Sci.* **60**, 34–51 (2012).

[3] Burr, D. M. *et al.* Fluvial features on Titan: Insights from morphology and modeling. *Geological Society of America Bulletin* **125**, 299–321 (2013).

[4] Neish, C. D. & Lorenz, R. D. Elevation distribution of Titan's craters suggests extensive wetlands. *Icarus* **228**, 27–34 (2014).

[5] Neish, C. D. *et al.* Fluvial erosion as a mechanism for crater modification on Titan. *Icarus* **270**, 114–129 (2016).

[6] Birch, S. *et al.* Geomorphologic mapping of Titan's polar terrains: Constraining surface processes and landscape evolution. *Icarus* **282**, 214–236 (2017).

[7] Stofan, E. R. *et al.* The lakes of Titan. *Nature* **445**, 61–64 (2007).

[8] Hayes, A. *et al.* Hydrocarbon lakes on Titan: Distribution and interaction with a porous regolith. *Geophys. Res. Lett.* **35**, L09204 (2008).

[9] Hayes, A. G. The lakes and seas of Titan. *Ann. Rev. Earth Planet. Sci.* **44**, 57–83 (2016).

[10] Hayes, A. *et al.* Topographic constraints on the evolution and connectivity of Titan's lacustrine basins. *Geophysical Research Letters* **44** (2017).

[11] Griffith, C. A. *et al.* The evolution of Titan's mid-latitude clouds. *Science* **310**, 474–477 (2005).

[12] Ádámkovics, M. *et al.* Meridional variation in tropospheric methane on Titan observed with AO spectroscopy at Keck and VLT. *Icarus* **270**, 376–388 (2016).

[13] Lora, J. M. & Ádámkovics, M. The near-surface methane humidity on Titan. *Icarus* **286**, 270–279 (2017).

[14] Mitchell, J. L. & Lora, J. M. The climate of Titan. *Ann. Rev. Earth Planet. Sci.* **44**, 353–380 (2016).

[15] Lora, J. M. & Mitchell, J. L. Titan's asymmetric lake distribution mediated by methane transport due to atmospheric eddies. *Geophys. Res. Lett.* **42**, 6213–6220 (2015).

[16] Perron, J. *et al.* Valley formation and methane precipitation rates on Titan. *J. of Geophys. Res. Planet.* **111**, E11 (2006).

[17] Jaumann, R. *et al.* Fluvial erosion and post-erosional processes on Titan. *Icarus* **197**, 526–538 (2008).

[18] Black, B., Perron, J., Burr, D. & Drummond, S. Estimating erosional exhumation on Titan from drainage network morphology. *J. of Geophys. Res. Planet.* **117**, E8 (2012).

[19] Birch, S., Hayes, A., Howard, A., Moore, J. & Radebaugh, J. Alluvial fan morphology, distribution and formation on Titan. *Icarus* **270**, 238–247 (2016).

[20] Faulk, S. P., Moon, S., Mitchell, J. L. & Lora, J. M. Regional patterns of extreme precipitation on Titan consistent with observed alluvial fan distribution. *Nature Geosci.* **10**, 827–831 (2017).

[21] Hayes, A. G. *et al.* Transient surface liquid in Titan's polar regions from Cassini. *Icarus* **211**, 655–671 (2011).

[22] Turtle, E. P., Perry, J. E., Hayes, A. G. & McEwen, A. S. Shoreline retreat at Titan's Ontario Lacus and Arrakis Planitia from Cassini Imaging Science Subsystem observations. *Icarus* **212**, 957–959 (2011).

[23] MacKenzie, S. M. *et al.* The case for seasonal surface changes at Titan's lake district. *Nature Astronomy* **3**, 506–510 (2019).

[24] Birch, S. *et al.* Morphological evidence that Titan's southern hemisphere basins are paleoseas. *Icarus* (2017).

[25] Turtle, E. P. *et al.* Titan's meteorology over the Cassini mission: Evidence for extensive subsurface methane reservoirs. *Geophys. Res. Lett.* **45**, 5320–5328 (2018).

[26] Lora, J. M., Lunine, J. I. & Russell, J. L. GCM simulations of Titan's middle and lower atmosphere and comparison to observations. *Icarus* **250**, 516–528 (2015).

[27] Mitchell, J. L. The drying of Titan's dunes: Titan's methane hydrology and its impact on atmospheric circulation. *J. Geophys. Res.* **113**, E08015 (2008).

[28] Schneider, T., Graves, S. D. B., Schaller, E. L. & Brown, M. E. Polar methane accumulation and rainstorms on Titan from simulations of the methane cycle. *Nature* **481**, 58–61 (2012).

[29] Tokano, T. Orbitally and geographically caused seasonal asymmetry in Titan's tropospheric climate and its implications for the lake distribution. *Icarus* **317**, 337–353 (2019).

[30] Horvath, D. G., Andrews-Hanna, J. C., Newman, C. E., Mitchell, K. L. & Stiles, B. W. The influence of subsurface flow on lake formation and north polar lake distribution on Titan. *Icarus* **277**, 103–124 (2016).

[31] Lopes, R. M. C. *et al.* Titan as revealed by the Cassini Radar. *Space Sci. Rev.* **215**, 33 (2019).

[32] Dhingra, R. D., Barnes, J. W., Yanites, B. J. & Kirk, R. L. Large catchment area recharges Titan's Ontario Lacus. *Icarus* **299**, 331–338 (2018).

[33] Corlies, P. *et al.* Titan's Topography and Shape at the End of the Cassini Mission. *Geophys. Res. Lett.* **44** (2017).

[34] Newman, C. E., Richardson, M. I., Lian, Y. & Lee, C. Simulating Titan's methane cycle with the TitanWRF general circulation model. *Icarus* **267**, 106–134 (2016).

[35] Mitchell, J. L., Pierrehumbert, R. T., Frierson, D. M. W. & Caballero, R. The dynamics behind Titan's methane clouds. *Proc. Natl. Acad. Sci.* **103**, 18421–18426 (2006).

[36] Jennings, D. E. *et al.* Titan surface temperatures during the Cassini mission. *Astrophys. J. Lett.* **877**, L8 (2019).

[37] Jennings, D. *et al.* Surface temperatures on Titan during northern winter and spring. *The Astrophysical Journal Letters* **816**, L17 (2016).

[38] Mitchell, J. L. Titan's transport-driven methane cycle. *Astrophys. J.* **756**, L26 (2012).

[39] Lora, J. M., Lunine, J. I., Russell, J. L. & Hayes, A. G. Simulations of Titan's paleoclimate. *Icarus* **243**, 264–273 (2014).

[40] Lorenz, R. D. *et al.* Titan's inventory of organic surface materials. *Geophys. Res. Lett.* **35**, L02206 (2008).

[41] Birch, S. P. D. *et al.* Raised rims around Titan's sharp-edged depressions. *Geophys. Res. Lett.* **45** (2018).

[42] Zarnecki, J. C. *et al.* A soft solid surface on Titan as revealed by the Huygens surface science package. *Nature* **438**, 792–795 (2005).

[43] Barnes, J. *et al.* Global-scale surface spectral variations on Titan seen from Cassini/VIMS. *Icarus* **186**, 242–258 (2007).

[44] Soderblom, L. *et al.* Correlations between Cassini VIMS spectra and RADAR SAR images: Implications for Titan's surface composition and the character of the Huygens Probe Landing Site. *Planet. Space Sci.* **55**, 2025–2036 (2007).

[45] Janssen, M. A. *et al.* Titan's surface at 2.18-cm wavelength imaged by the Cassini RADAR radiometer: Results and interpretations through the first ten years of observation. *Icarus* **270**, 443–459 (2016).

[46] Griffith, C. A. *et al.* A corridor of exposed ice-rich bedrock across Titan's tropical region. *Nature Astronomy* (2019).

[47] Cornet, T. *et al.* Dissolution on Titan and on Earth: Toward the age of Titan's karstic landscapes. *Journal of Geophysical Research: Planets* **120**, 1044–1074 (2015).

[48] Lopes, R. M. *et al.* Nature, distribution, and origin of Titan's Undifferentiated Plains. *Icarus* **270**, 162–182 (2016).

[49] Tobie, G., Lunine, J. I. & Sotin, C. Episodic outgassing as the origin of atmospheric methane on Titan. *Nature* **440**, 61–64 (2006).

[50] Mousis, O., Choukroun, M., Lunine, J. I. & Sotin, C. Equilibrium composition between liquid and clathrate reservoirs on Titan. *Icarus* **239**, 39–45 (2014).

[51] Frierson, D. The dynamics of idealized convection schemes and their effect on the zonally averaged tropical circulation. *J. Atmos. Sci.* **64**, 1959–1976 (2007).

[52] Philip, J. R. Evaporation, and moisture and heat fields in the soil. *Journal of meteorology* **14**, 354–366 (1957).

[53] Shah, N., Nachabe, M. & Ross, M. Extinction depth and evapotranspiration from ground water under selected land covers. *Groundwater* **45**, 329–338 (2007).

[54] Johnson, E., Yáñez, J., Ortiz, C. & Muñoz, J. Evaporation from shallow groundwater in closed basins in the Chilean Altiplano. *Hydrological Sciences Journal–Journal des Sciences Hydrologiques* **55**, 624–635 (2010).

[55] Kurc, S. A. & Small, E. E. Dynamics of evapotranspiration in semiarid grassland and shrubland ecosystems during the summer monsoon season, central New Mexico. *Water Resources Research* **40** (2004).

[56] Tokano, T. Meteorological assessment of the surface temperatures on Titan: constraints on the surface type. *Icarus* **173**, 222–242 (2005).

[57] MacKenzie, S. M., Lora, J. M. & Lorenz, R. D. A thermal inertia map of Titan. *J. Geophys. Res. Planet.* **124** (2019).

[58] Cammeraat, E. L. Scale dependent thresholds in hydrological and erosion response of a semi-arid catchment in southeast Spain. *Agriculture, Ecosystems & Environment* **104**, 317–332 (2004).

606 [59] O'Callaghan, J. F. & Mark, D. M. The extraction of drainage networks from digital
607 elevation data. *Computer Vision, Graphics, and Image Processing* **28**, 323–344 (1984).

608 [60] Tarboton, D. G. A new method for the determination of flow directions and upslope
609 areas in grid digital elevation models. *Water Resources Research* **33**, 309–319 (1997).

610 [61] Freeman, T. G. Calculating catchment area with divergent flow based on a regular grid.
611 *Computers & Geosciences* **17**, 413–422 (1991).

612 [62] Shelef, E. & Hilley, G. E. Impact of flow routing on catchment area calculations, slope
613 estimates, and numerical simulations of landscape development. *Journal of Geophysical*
614 *Research: Earth Surface* **118**, 2105–2123 (2013).

615 [63] Overton, D. Route or convolute? *Water Resources Research* **6**, 43–52 (1970).

616 [64] Watt, W. E. & Chow, K. A. A general expression for basin lag time. *Canadian Journal*
617 *of Civil Engineering* **12**, 294–300 (1985).

618 [65] Liston, G., Sud, Y. & Wood, E. Evaluating GCM land surface hydrology parameteri-
619 zations by computing river discharges using a runoff routing model: Application to the
620 Mississippi basin. *Journal of Applied Meteorology* **33**, 394–405 (1994).

621 [66] Miller, J. R., Russell, G. L. & Caliri, G. Continental-scale river flow in climate models.
622 *Journal of Climate* **7**, 914–928 (1994).

623 [67] Coe, M. T. Modeling terrestrial hydrological systems at the continental scale: Testing
624 the accuracy of an atmospheric GCM. *Journal of Climate* **13**, 686–704 (2000).

625 [68] Wang, J. *et al.* The coupled routing and excess storage (CREST) distributed hydrolog-
626 ical model. *Hydrological Sciences Journal* **56**, 84–98 (2011).

627 [69] Askew, A. J. Derivation of formulae for variable lag time. *Journal of Hydrology* **10**,
628 225–242 (1970).

629 [70] Singh, V. P. Hydrologic systems. Volume I: Rainfall-runoff modeling. *Prentice Hall,*
630 *Englewood Cliffs New Jersey. 1988. 480* (1988).

[71] Vörösmarty, C. J. *et al.* Continental scale models of water balance and fluvial transport: An application to South America. *Global Biogeochemical Cycles* **3**, 241–265 (1989).

[72] Sellers, P. *et al.* A revised land surface parameterization (SiB2) for atmospheric GCMs. part I: Model formulation. *Journal of climate* **9**, 676–705 (1996).

[73] Milly, P. *et al.* An enhanced model of land water and energy for global hydrologic and earth-system studies. *Journal of Hydrometeorology* **15**, 1739–1761 (2014).

[74] Iess, L. *et al.* The tides of Titan. *Science* **337**, 457–459 (2012).

SUPPLEMENTARY INFORMATION

Climate patterns and surface methane distribution explained by coupling of land hydrology and atmosphere in Titan's methane cycle

Sean P. Faulk[1†], Juan M. Lora[1,2†*], Jonathan L. Mitchell[1,3], P.C.D. Milly[4]

[1]Department of Earth, Planetary, and Space Sciences, University of California, Los Angeles, CA
[2]Department of Geology and Geophysics, Yale University, New Haven, CT
[3]Department of Atmospheric and Oceanic Sciences, University of California, Los Angeles, CA
[4]US Geological Survey, Princeton, NJ

[†]Equal-contribution authors
[*]Corresponding author: juan.lora@yale.edu

Supplementary Figures

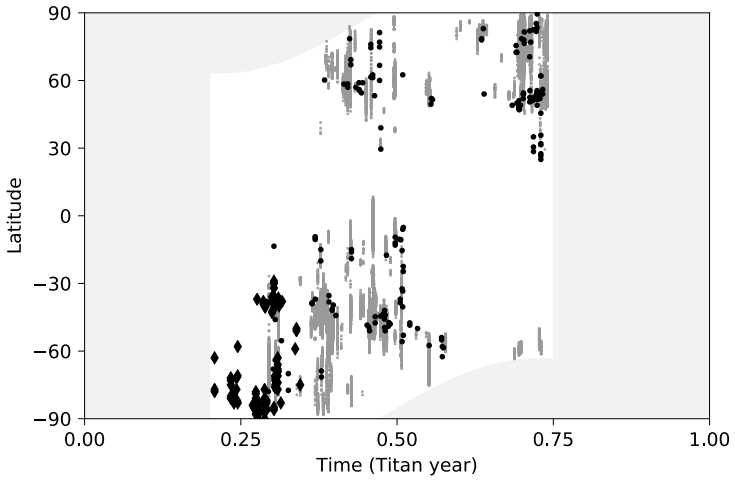

Supplementary Figure 1: Observed clouds. Latitudes of observations of Titan's seasonally-evolving tropospheric clouds as a function of the fraction of Titan's year for comparison to Fig. 5. Diamonds show ground-based observations [1–3]; gray and black circles show Cassini VIMS and ISS observations, respectively [4]. Times of the year where no observations are available are shaded light gray. Note that high latitude late winter and early spring clouds are small-scale clouds [5] that may not precipitate, and therefore cannot be directly compared to the model.

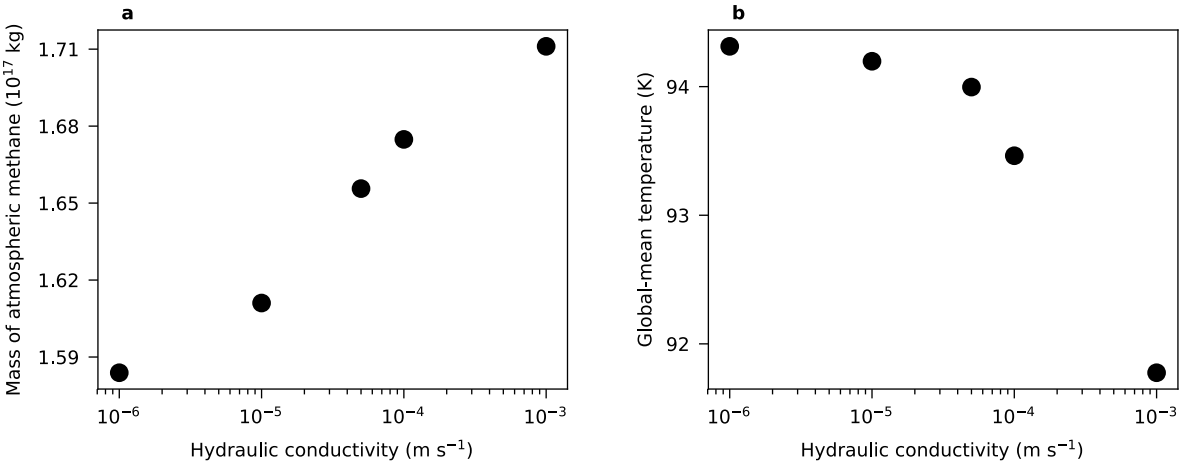

Supplementary Figure 2: Methane reservoirs. a) Total mass of atmospheric methane vapor as a function of the simulations' hydraulic conductivity k. b) Globally and seasonally averaged surface temperatures as a function of the simulations' hydraulic conductivity k.

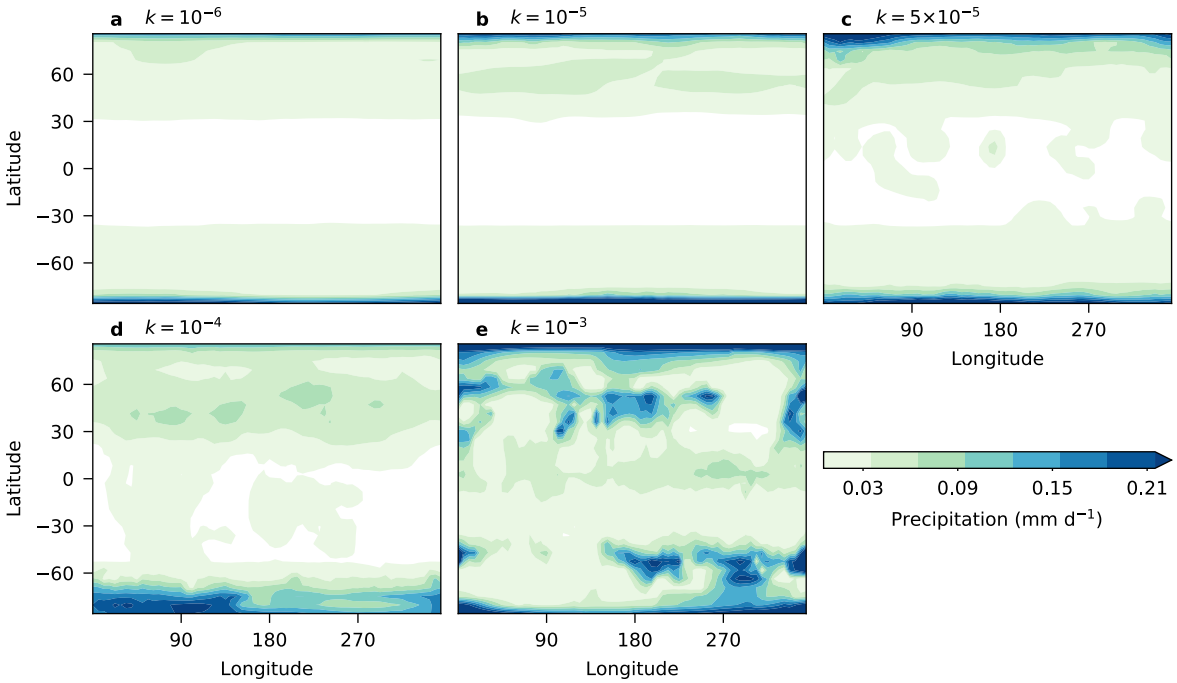

Supplementary Figure 3: Precipitation. Maps of the average precipitation (mm d^{-1}) over the final 20 Titan years of each simulation. The hydraulic conductivity k of the surface (in units of m s^{-1}) is shown for each case, and corresponds to a permeability of a) 10^{-8} cm^2, b) 10^{-7} cm^2, c) 5×10^{-7} cm^2, d) 10^{-6} cm^2, and e) 10^{-5} cm^2.

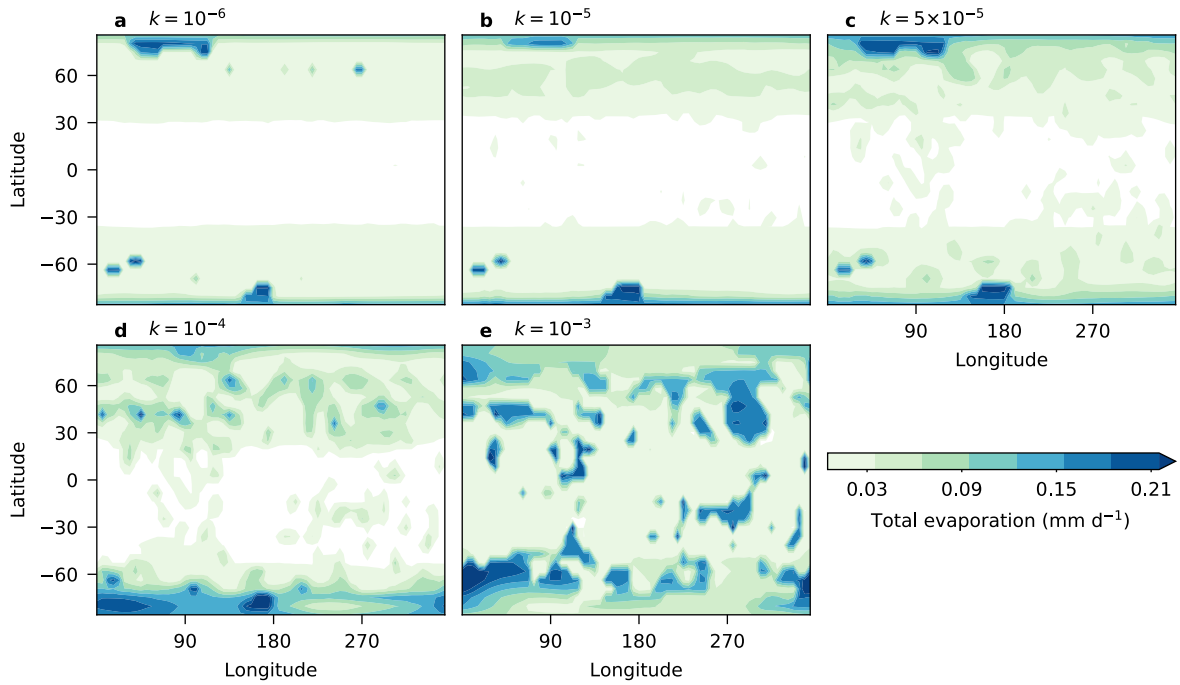

Supplementary Figure 4: Total evaporation. Maps of the average total evaporation (that is, including groundmethane evaporation as well as evaporation from the surface; mm d^{-1}) over the final 20 Titan years of each simulation. Simulations as in Supplementary Fig. 3.

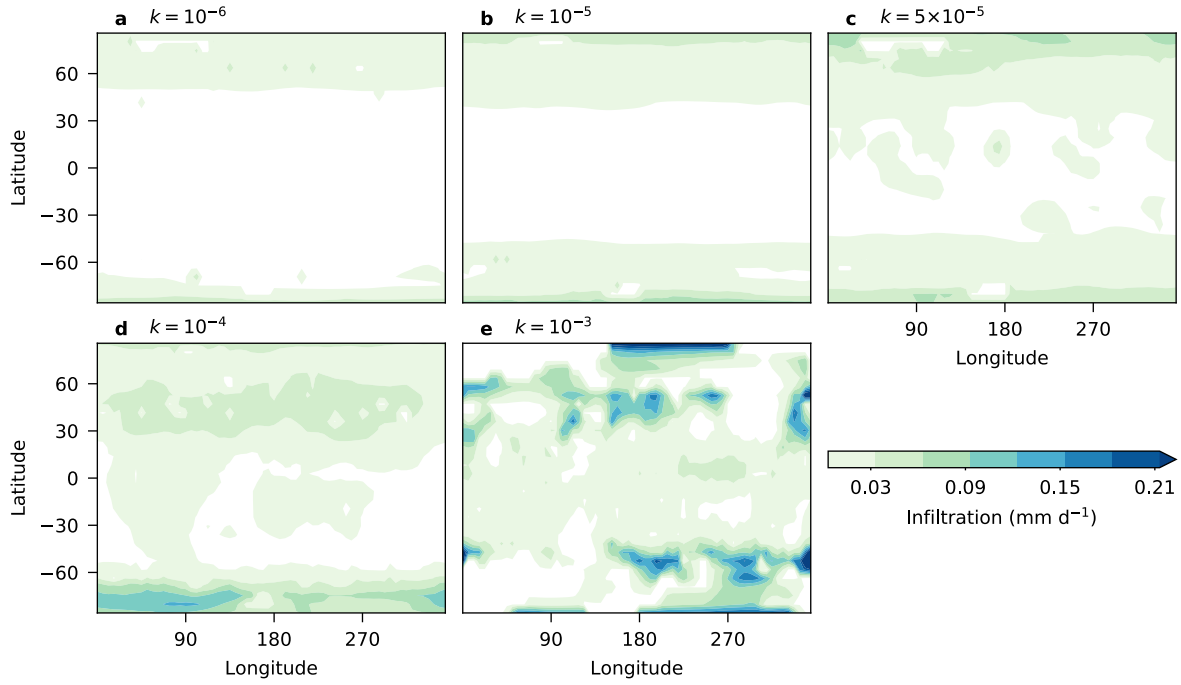

Supplementary Figure 5: Infiltration. Maps of the average infiltration (mm d^{-1}) over the final 20 Titan years of each simulation. Simulations as in Supplementary Fig. 3.

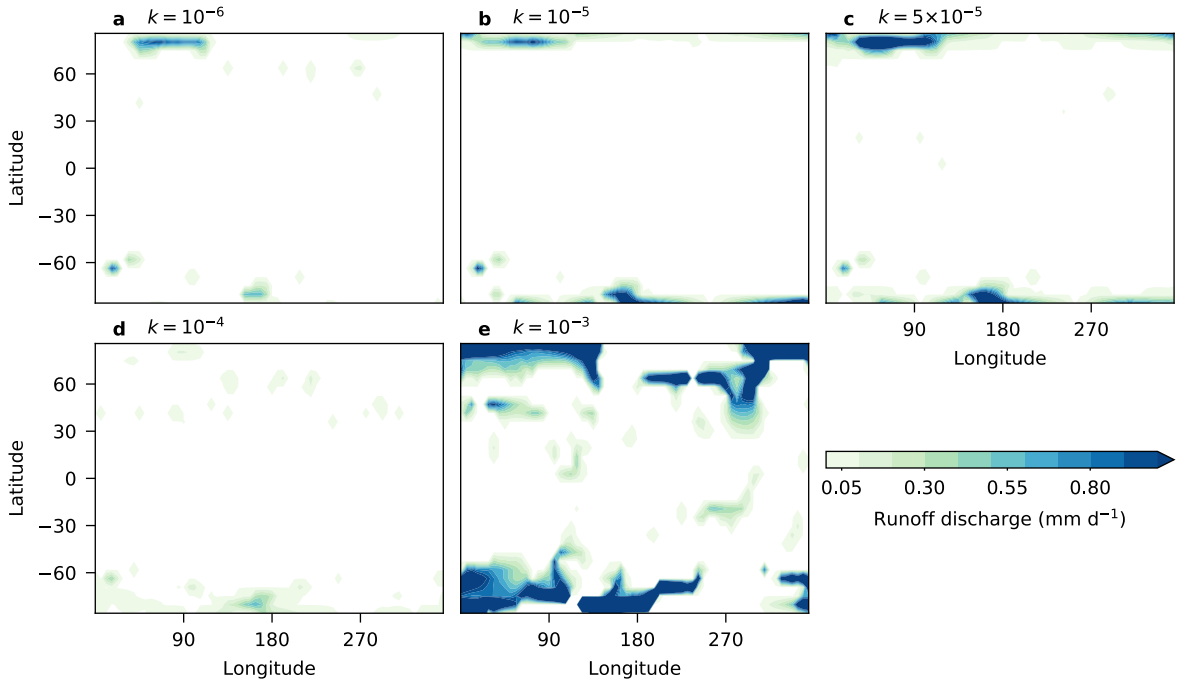

Supplementary Figure 6: Runoff discharge. Maps of the average runoff discharge into the surface reservoir (mm d^{-1}) over the final 20 Titan years of each simulation. Simulations as in Supplementary Fig. 3.

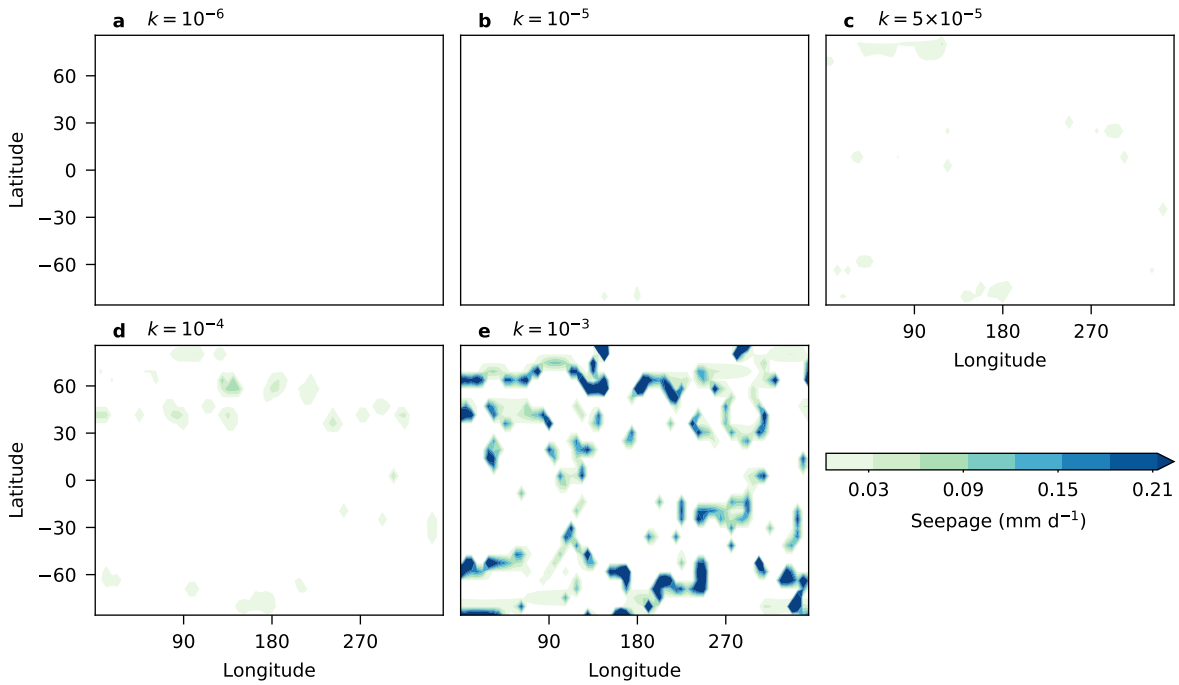

Supplementary Figure 7: Seepage. Maps of the average seepage from the methane table (mm d^{-1}) over the final 20 Titan years of each simulation. Simulations as in Supplementary Fig. 3.

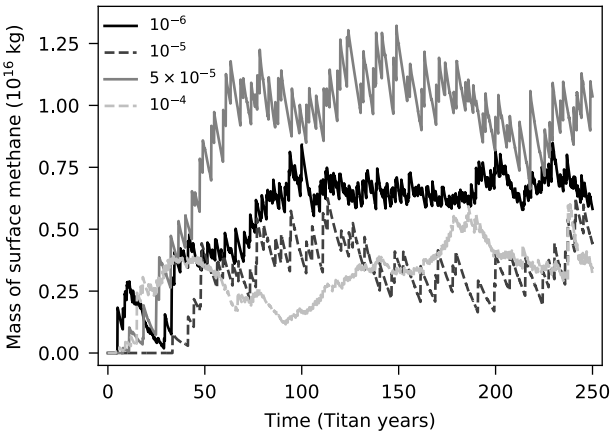

Supplementary Figure 8: Evolution of surface methane. Total mass of surface methane in the simulations with $k \leq 10^{-4}$ m s^{-1} (curve labels show k) over the course of each simulation. The simulation with $k = 10^{-3}$ m s^{-1} is not shown.

References

[1] Bouchez, A. H. & Brown, M. E. Statistics of Titan's south polar tropospheric clouds. *Astrophys. J.* **618**, L53–L56 (2005).

[2] Roe, H. G., Brown, M. E., Schaller, E. L., Bouchez, A. H. & Trujillo, C. A. Geographic control of Titan's mid-latitude clouds. *Science* **310**, 477–479 (2005).

[3] Schaller, E. L., Brown, M. E., Roe, H. G., Bouchez, A. H. & Trujillo, C. A. Dissipation of Titan's south polar clouds. *Icarus* **184**, 517–523 (2006).

[4] Turtle, E. P. *et al.* Titan's meteorology over the Cassini mission: Evidence for extensive subsurface methane reservoirs. *Geophys. Res. Lett.* **45**, 5320–5328 (2018).

[5] Brown, M. E. *et al.* Discovery of lake-effect clouds on Titan. *Geophys. Res. Lett.* **36**, L01103 (2009).